sensors

MDPI

Article

The Wavelength-Shifting Optical Module

Benjamin Bastian-Querner [1], Lucas S. Binn [2], Sebastian Böser [2], Jannes Brostean-Kaiser [1,3], Dustin Hebecker [1,3], Klaus Helbing [4], Timo Karg [3], Lutz Köpke [2], Marek Kowalski [1,3], Peter Peiffer [2], Anna Pollmann [4,*], John Rack-Helleis [2], Martin Rongen [2], Lea Schlickmann [2], Florian Thomas [2] and Anna Vocke [2]

1 Institut für Physik, Humboldt-Universität zu Berlin, 12489 Berlin, Germany; benjamin.bastian@desy.de (B.B.-Q.); jannes@physik.hu-berlin.de (J.B.-K.); dustin.hebecker@gmail.com (D.H.); marek.kowalski@desy.de (M.K.)
2 Institute of Physics, University of Mainz, Staudinger Weg 7, 55099 Mainz, Germany; lbinn@students.uni-mainz.de (L.S.B.); sboeser@uni-mainz.de (S.B.); lutz.koepke@uni-mainz.de (L.K.); peter.peiffer@gmail.com (P.P.); jorackhe@uni-mainz.de (J.R.-H.); mrongen@uni-mainz.de (M.R.); lea.schlickmann@rwth-aachen.de (L.S.); fthomas@uni-mainz.de (F.T.); asteuer@icecube.wisc.edu (A.V.)
3 Deutsches Elektronen-Synchrotron (DESY), 15738 Zeuthen, Germany; timo.karg@desy.de
4 Department of Physics, University of Wuppertal, 42119 Wuppertal, Germany; helbing@uni-wuppertal.de
* Correspondence: anna.pollmann@uni-wuppertal.de

Abstract: The Wavelength-shifting Optical Module (WOM) is a novel photosensor concept for the instrumentation of large detector volumes with single-photon sensitivity. The key objective is to improve the signal-to-noise ratio, which is achieved by decoupling the photosensitive area of a sensor from the cathode area of its photomultiplier tube (PMT). The WOM consists of a transparent tube with two PMTs attached to its ends. The tube is coated with wavelength-shifting paint that absorbs ultraviolet photons with nearly 100% efficiency. Depending on the environment, e.g., air (ice), up to 73% (41%) of the subsequently emitted optical photons can be captured by total internal reflection and propagate towards the PMTs, where they are recorded. The optical properties of the paint, the geometry of the tube, and the coupling of the tube to the PMTs have been optimized for maximal sensitivity based on theoretical derivations and experimental evaluations. Prototypes were built to demonstrate the technique and to develop a reproducible construction process. Important measurable characteristics of the WOM are the wavelength-dependent effective area, the transit time spread of detected photons, and the signal-to-noise ratio. The WOM outperforms bare PMTs, especially with respect to the low signal-to-noise ratio with an increase of a factor up to 8.9 in air (5.2 in ice). Since the gain in sensitivity is mostly in the UV regime, the WOM is an ideal sensor for Cherenkov and scintillation detectors.

Keywords: neutrino detectors; photon detection; wavelength-shifting; UV sensitivity; low noise; large sensitive area; photomultiplier tubes

Citation: Bastian-Querner, B.; Binn, L.S.; Böser, S.; Brostean-Kaiser, J.; Hebecker, D.; Helbing, K.; Karg, T.; Köpke, L.; Kowalski, M.; Peiffer, P.; et al. The Wavelength-Shifting Optical Module. *Sensors* **2022**, *22*, 1385. https://doi.org/10.3390/s22041385

Academic Editor: Vittorio M.N. Passaro

Received: 25 December 2021
Accepted: 28 January 2022
Published: 11 February 2022

1. Introduction

Many detectors for rare events in particle and astroparticle physics require large interaction volumes, ranging up to cubic kilometers, in order to achieve a reasonable detection rate. However, the larger the volume, the smaller the feasible density of instrumentation. A viable method for reading out detectors with transparent target media is the detection of optical photons emitted by incident particles (or their secondaries) in the form of Cherenkov emission or scintillation light. The prevailing sensor types that are capable of detecting *single photons* are photomultiplier tubes (PMTs). They are, for example, deployed in neutrino telescopes, neutrino detectors, and dark matter experiments, such as IceCube [1], Super-Kamiokande [2], Borexino [3], SNO [4], JUNO [5], XENON [6], LUX [7], DARWIN [8], and many others. The photosensitive area of a PMT scales approximately linearly with the area of its photocathode, as does the dark current—the dominant source of noise. The

peak quantum efficiency of conventional PMTs is around 450 nm, which is suboptimal for Cherenkov light, as well as for scintillation emissions from common liquid scintillators based on linear alkylbenzene (LAB) at approximately 340 nm [9] or liquid noble gases, such as xenon or argon, at around 178 nm and 128 nm, respectively.

The wavelength-shifting optical module (WOM) has been developed as an alternative sensor for large volume detectors. The WOM, schematically shown in Figure 1, consists of a transparent tube with photosensors attached to its ends. The tube is coated with a paint containing wavelength-shifting (WLS) organic luminophores and acts as a light collector. The delayed isotropic emission of the WLS molecules circumvents the conservation of phase space as required by Liouville's theorem (etendue), which otherwise forbids the concentration of a homogeneous light distribution in a smaller area using refractive and reflective optics.

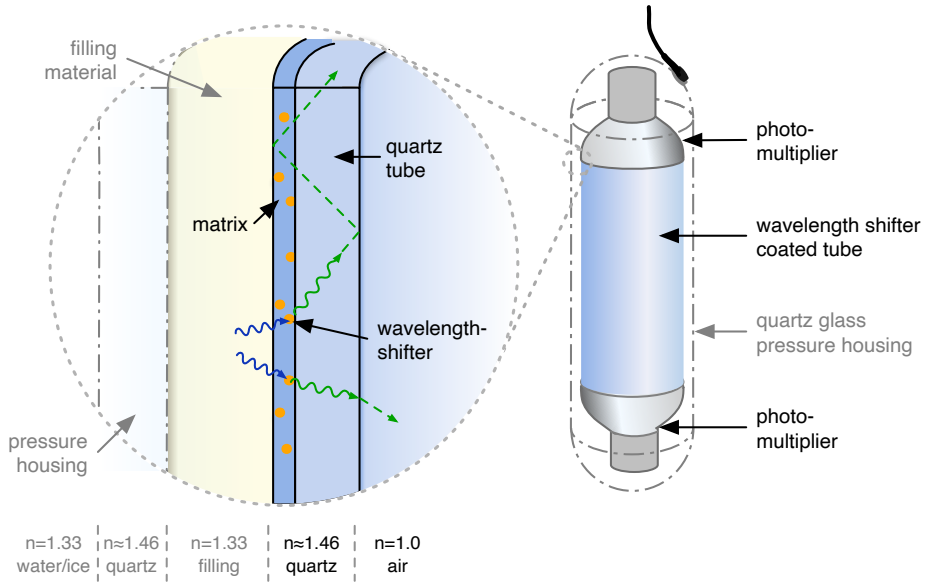

Figure 1. A schematic drawing of the WOM. UV photons are absorbed in the WLS paint layer and are re-emitted as optical photons. If the emission angle of the photons is larger than the critical angle, they are trapped by total internal reflection and are guided along the tube to small, low-noise PMTs.

The performance of the WOM is determined by a number of efficiency factors, which are discussed throughout this work. The overall efficiency of the WOM ϵ_{tot} is defined as the number of detected photons N_{det} compared to the number of incident photons N_{inc} as follows:

$$\epsilon_{\text{tot}} = \frac{N_{\text{det}}}{N_{\text{inc}}} = \epsilon_{\text{LY}}^{\text{WLS}}(\lambda_{\text{inc}}) \cdot \epsilon_{\text{TIR}}(x_0) \cdot \epsilon_{\text{TP}}(z) \cdot \epsilon_{\text{QE}}^{\text{PMT}}(\lambda_{\text{em}}) \cdot \epsilon_{\text{IF}} \cdot \epsilon_{\text{TM}}(\lambda_{\text{inc}}) \tag{1}$$

UV photons incident on the WLS tube are absorbed in the paint layer and re-emitted isotropically as optical photons with the light yield $\epsilon_{\text{LY}}^{\text{WLS}}$. This efficiency depends on the wavelength of the incident photons λ_{inc}, as well as the thickness of the paint layer d and the concentration of wavelength-shifting molecules c_{WLS}. Values close to unity can be achieved over a large part of the absorption spectrum. A fraction ϵ_{TIR} of the re-emitted photons have an angle with the tube wall smaller than the critical angle for total internal reflection (TIR). The radial symmetry of the configuration ensures that the photon incidence angle on the surface remains constant for each interaction. Therefore, subsequent surface interactions also fulfill the TIR criterion, such that the photons are trapped and guided towards the ends of the tube; see Figure 2. The TIR fraction ϵ_{TIR} depends on the fraction of the tube's radius x_0 at which the photons are emitted, as well as on the refractive indices of the tube n_{tube} and the environment n_{env}, which define the critical angle.

While the captured photons are propagating towards the ends of the tube, they can be absorbed or scattered out of the material. This attenuation effect, denoted as ϵ_{TP}, depends on the distance z between the emission point and the end of the tube, as well as the scattering λ_{scatt} and absorption length λ_{abs} (merged into the attenuation length λ_{att}). Attached to the tube are PMTs that are characterized by their wavelength-dependent quantum efficiency $\epsilon_{\mathrm{QE}}^{\mathrm{PMT}}$, which depends on the wavelength of the re-emitted photons λ_{em}. A small fraction of photons are lost at the tube–PMT interface, which is denoted as ϵ_{IF}.

In some environments, it is necessary to encapsulate the WOM with a housing, e.g., in deep water or ice, to protect the WOM from pressure. The probability for transmission into the housing through an optional filling into the WOM ϵ_{TM} depends on the wavelength λ_{inc} of the incident photons and the refractive indices $n_{\mathrm{env}}, n_{\mathrm{housing}}, n_{\mathrm{fill}}$ of the materials enclosing the WLS tube.

All of the efficiencies described above are used to characterize the WOM in this paper. As a baseline in this paper, the following *prototype design* is discussed: The tube, coated on the inside surface with wavelength-shifting paint, is 700 mm long, made of quartz [10] with an outer diameter of 60 mm and a wall thickness of 2.5 mm. Two 3.5 inch PMTs [11] are attached to the ends with optical gel [12]. An optional quartz pressure vessel (the dimensions of this pressure vessel are given by availability in the laboratory; the dimensions of the WOM tube and the PMT diameters are derived from these) is added around the WOM with 1200 mm length, 110 mm outer diameter, and 10 mm wall thickness. The dimensions and materials of any setup discussed in this text correspond to this prototype design—apart from a few exceptions, which are described accordingly.

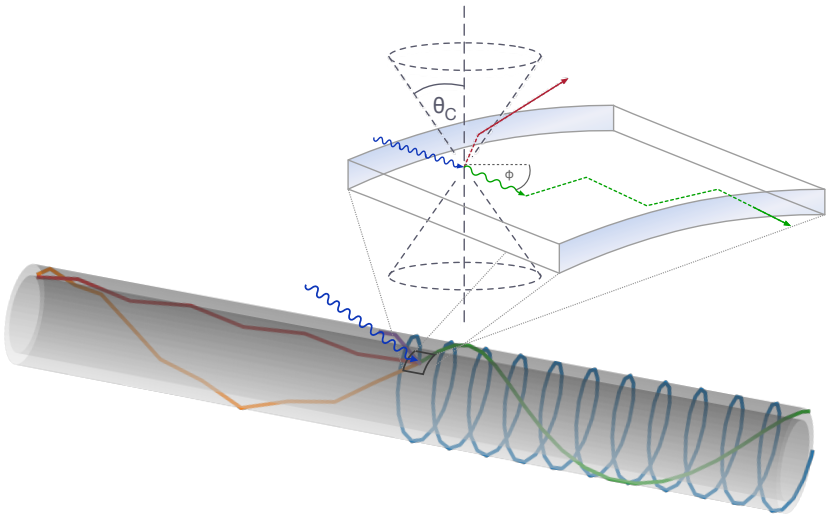

Figure 2. Visualization of several photon paths propagating in the wall of the WOM tube simulated with a GPU-based ray-tracing algorithm [13]. The photons are generated inside the paint layer of the tube in response to the incident UV photons (blue). Their attenuation probability depends on the effective path length, which, in turn, depends on the emission angle. In the inset, a UV photon (blue) is shown, which is absorbed and re-emitted in the material (green) or lost (red). The critical angle for the re-emitted photon defines a *loss cone* (gray dashed lines).

In this paper, the different optical processes required to describe and optimize the efficiency of the WOM are discussed in Section 2. The optimized production of the main component of the WOM, the coating of the wavelength-shifting tube, is described in Section 3. Finally, characterization and performance measurements of the WOM are presented in Section 4.

2. Performance Factors

The efficiencies of the WOM components, which make up the overall efficiency of the WOM, as introduced in Equation (1), are derived in this chapter.

2.1. Total Internal Reflection

The concept of the WOM revolves around the idea of total internal reflection of photons if the difference in refractive indices between the tube n_{tube} and the surrounding environment n_{env} is large (since a hollow tube is coated on one surface side, it is the lower of the refractive indices of the wavelength-shifting paint n_{paint} and the coated substrate $n_{\text{substrate}}$ that determines the critical angle, i.e., $n_{\text{tube}} = \min(n_{\text{paint}}, n_{\text{substrate}})$. Using the Fresnel equation for the reflectivity of an electromagnetic wave $R(\theta, n_{\text{paint}}, n_{\text{env}})$ for a re-emitted photon incident on the surface, the fraction of captured photons after N interactions with the surface can be determined as

$$\epsilon_{\text{TIR}} = \frac{1}{2} \int \left(R(\theta, n_{\text{paint}}, n_{\text{env}})\right)^N \sin\theta \, d\theta \tag{2}$$

where θ is the angle of the photon trajectory $\vec{p}$ to the surface normal $\vec{n}$; hence, $\cos\theta = \vec{p} \cdot \vec{n}$. In contrast to mirroring surfaces that achieve typical average reflectance of 90–99% if employed over a larger wavelength range, the TIR above the critical angle $\sin\theta_{\text{crit}} = n_{\text{env}}/n_{\text{tube}}$ reaches 100% reflectance independently of the wavelength. In the limit of a large number of interactions, the reflectance R can be approximated by a step-function Θ, and Equation (2) simplifies to

$$\lim_{N\to\infty} \varepsilon_{\text{TIR}} = \frac{1}{2} \int \Theta(\cos\theta - \cos\theta_{\text{crit}}) \sin\theta \, d\theta = \cos\theta_{\text{crit}} \tag{3}$$

The critical angle thus defines two sharp loss cones, while all other photons are captured; see Figure 2. In the configurations discussed here, neither the tube material nor the wavelength-shifting paint or surrounding environment exhibit strong dispersion, so that $\epsilon_{\text{TIR}} \simeq 73\%$ ($\theta_{\text{crit}} \simeq 43.2^\circ$) for a WOM tube ($n_{\text{tube}} \simeq 1.46$) operated in air ($n \simeq 1.0$) and $\epsilon_{\text{TIR}} \simeq 41\%$ ($\theta_{\text{crit}} \simeq 65.6^\circ$) for a WOM tube operated in water ($n \simeq 1.33$). The surface curvature given by the radius of the tube r_{tube} was neglected, which is a good approximation as long as the radius of the emission point r_{em} is close to the surface $r_{\text{tube}} - r_{\text{em}} \ll r_{\text{tube}}$ (denoted as *no-curvature* approximation later on). In resorting to the ray-like description of reflectance, evanescence was also neglected, which is a good approximation as long as the emission point is further away from the surface than the typical wavelength $r_{\text{tube}} - r_{\text{em}} \gg \lambda_{\text{em}}$. Both conditions are well satisfied in the given configuration with a typical emission wavelength of 400 nm to 500 nm, coating thicknesses $r_{\text{tube}} - r_{\text{em}}$ in the range of several micrometers, and tube radii r_{tube} of several centimeters. The TIR efficiency ϵ_{TIR} is thus independent of the tube radius r_{tube} in good approximation.

While the general working principle of the WOM is similar to that of a wavelength-shifting fiber, the different geometry makes a noteworthy difference in the fraction of photons that can be captured by total internal reflection. Following a purely geometrical argument, there is no difference between a hollow tube and a solid cylinder, as for any photon trajectory, the incidence angle on the inner surface of a hollow tube will always be larger than the incidence angle on the outer surface. Total internal reflection in the first interaction on the outer surface is thus a fully sufficient criterion to determine whether a photon is captured and guided along the tube. In a full cylinder, the *no-curvature* approximation $r_{\text{tube}} - r_{\text{em}} \ll r_{\text{tube}}$ no longer applies, and Equation (3) needs to be generalized to

$$\varepsilon_{\text{TIR}} = \frac{1}{4\pi} \int \Theta(|\vec{p} \cdot \vec{n}| - \cos(\theta_{\text{crit}})) \, d\Omega \tag{4}$$

If the emission point $\vec{r}_{\text{em}}$ sits in the center of the cylinder—as would approximately be the case in a wavelength-shifting fiber—this results in two symmetrical *capture cones* along the symmetry axis of the fiber, while most of the photons are lost even for large values of θ_{crit} (left-most case in Figure 3). As the emission point is moved outward by a fraction $x_0 = r_{\text{em}}/r_{\text{tube}}$, the incidence angle for photons orthogonal to the offset vector of the emission point $\vec{p} \perp \vec{r}_{\text{em}}$ increases, thus increasing the overall capture fraction. Moving the emission point out to $x_o = \sin(\theta_c)$, even *horizontal* photons $\vec{p} \perp \vec{r}_{\text{em}} \perp \vec{z}$ that are also

perpendicular to the cylinder axis $\vec{z}$ subtend an angle larger than the critical angle with the surface so that, under some azimuthal angle, all photons are captured independently of their polar angle. This region is maximized for emission on the surface, $\lim x_0 \to 1$, where, again, only the two cones around the surface normal vector are lost. This is the edge case depicted in Figure 2 close to which the WOM is operated. In Figure 4, the fraction of the solid angle ϵ_{TIR} under which the light is captured in the first surface interaction is shown. For the ease of handling and to protect the coating from the environment, the coating is applied on the inside of the prototype discussed here. In this case, x_0 and, thus, the wall thickness of the tube become relevant parameters. For the particular geometry of the prototype, significant losses due to x_0 only occur if the module is immersed in water or ice.

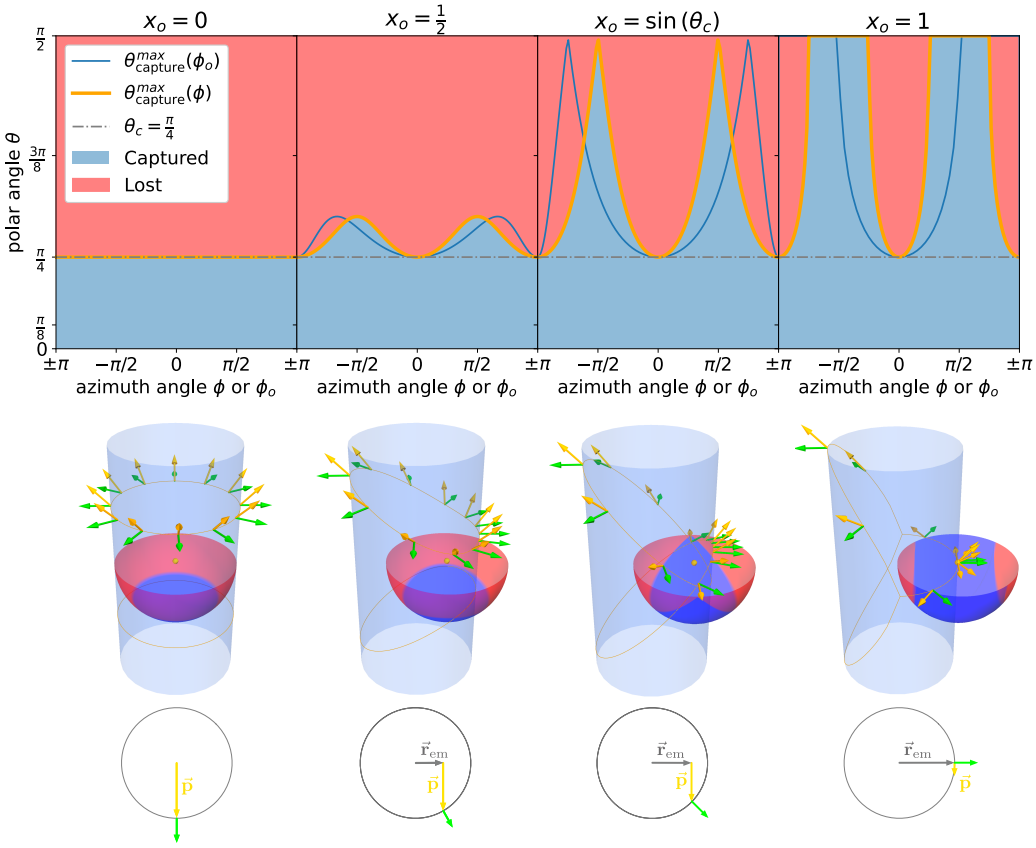

Figure 3. Illustration of the solid angle under which the photons are captured as a function of the relative fraction of the radius $x_0 = |\vec{r}|/R$ at which the photons are emitted (indicated by the yellow dot). The orange (blue) line in the upper plot indicates photons that encounter the surface under the critical angle as a function of the azimuth angle ϕ (ϕ_0) relative to the emission point (center of the cylinder). In the upper and middle plots, the blue shaded areas indicate solid angle regions under which photon trajectories are captured by total internal reflection, while red shaded areas show those that are not captured. In the middle plot, yellow arrows indicate directions of incident photons, while green arrows depict surface normals. In this example, the critical angle is chosen as $\theta_c = \pi/4$.

2.2. Light Propagation

Once the photons are trapped in the tube, absorption and scattering are the two mechanisms that contribute to light losses along the photon path with characteristic lengths λ_{abs} and λ_{scatt}. While absorbed photons are lost directly, scattered photons may no longer be confined by total internal reflection, leading to a total attenuation characterized by the attenuation length λ_{att}. Both attenuation mechanisms depend on the photon path length, which, in turn, depends on the initial emission direction (see Figure 2).

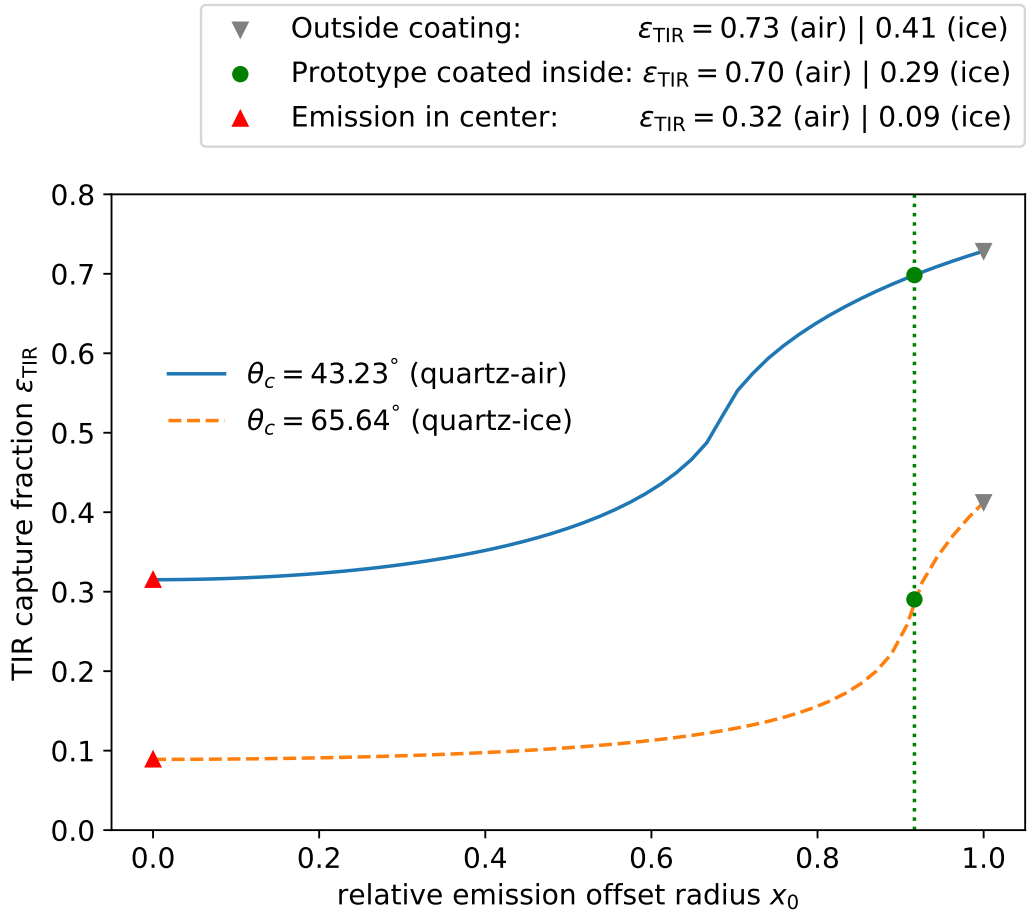

Figure 4. Fraction ϵ_{TIR} of the solid angle under which emitted photons are captured by total internal reflection as a function of the offset radius x_0 of the emission point. The two lines represent a module immersed in air (solid) or water (dashed). The green dots indicated the captured efficiency for the prototype module, which is coated on the inside of tube. Minimal values for the emission point in the center of the tube and maximal values for emission on the outside of the tube are indicated by triangles.

Using the *no-curvature* approximation from above as a basis, the path length distribution can be described in an analytical model—the so-called *flattened model*. Therein, the tube mantle is approximated as a flat rectangle with periodic boundary conditions on the long sides. (Figuratively, the mantle is 'cut open' and flattened out, and photons reaching one of the long sides of the rectangle enter it again from the opposite side.) In addition to the (polar) surface incidence angle θ, the azimuthal angle ϕ is defined, with $\phi = 0$ denoting the direction towards one end of the flattened tube (see Figure 2). Due to the symmetry of the situation, it is sufficient to consider photons that travel towards one end, limiting ϕ to the range $[-\pi/2, \pi/2]$. In the *flattened model*, the path length to the end of the tube becomes $z/(\cos(\phi)\cos(\theta))$, and the one-sided efficiency (i.e., the fraction of re-emitted photons reaching one end of the tube) is calculated as

$$\epsilon_{\mathrm{one-sided}}(z, \lambda_{\mathrm{att}}) := \epsilon_{\mathrm{TIR}} \cdot \epsilon_{\mathrm{TP}}(z, \lambda_{\mathrm{att}}) = \frac{1}{4\pi} \cdot \int_{-\pi/2}^{\pi/2} \int_{-\theta_C}^{\theta_C} \exp\left(-\frac{z}{\cos(\phi)\cos(\theta)\,\lambda_{\mathrm{att}}}\right) \cos(\theta)\, d\theta\, d\phi \quad (5)$$

Since $\epsilon_{\mathrm{LY}}^{\mathrm{WLS}} \approx 1 \approx \epsilon_{\mathrm{IF}}$ in Equation (1), the one-sided efficiency becomes the predominant performance measure differentiating the WOM from the operation of a bare PMT. The shape of this distribution can be seen in Figure 12, where it is fit to measurements.

To verify this simplistic model, it is compared to a Monte Carlo (MC) simulation of the photon propagation in the tube. The GPU-based implementation incorporates the

full 3D geometry, as well as an accurate model of absorption and scattering [13]; see the visualization in Figure 2. The model and the simulation agree with less than <1% deviation for a tube length of 20 mm to 1200 mm. Therefore, further MC simulations used in this work use the model instead of the GPU simulation.

2.3. Light Transmission

If the WOM is operated in a pressure housing with refractive index n_{housing}, the transmission of light from the environment with refractive index n_{env} into the modules needs to be taken into account. In order to preserve the UV sensitivity, quartz glass can be used. The extinction coefficient is less than 0.1% per centimeter down to a wavelength of $\lambda_{\text{inc}} \sim 180\,\text{nm}$ for fused silica and down to $\lambda_{\text{inc}} \sim 240\,\text{nm}$ for fused quartz [14], so the dependence on the photon wavelength λ_{inc} can be neglected in most cases.

There are two processes that compete while optimizing the refractive index of the *filling material* n_{fill} between the housing and the WOM tube: (i) Materials with low refractive index will optimize the capture efficiency ϵ_{TIR} (see Equation (3)), while (ii) they reduce the the efficiency of photon transmission ϵ_{TM} into the module due to total internal reflection at the housing–filling material boundary. In the co-planar model with isotropic illumination, the capture efficiency $\epsilon_{\text{comb}}^{\text{co-planar}}$ is derived from the Fresnel equations

$$\begin{aligned}\epsilon_{\text{comb}}^{\text{co-planar}}(n_{\text{env}}, n_{\text{fill}}) :&= \epsilon_{\text{TM}}(n_{\text{env}}, n_{\text{housing}}, n_{\text{fill}}) \cdot \epsilon_{\text{TIR}}(n_{\text{fill}}, n_{\text{tube}}) \\ &= \int_0^{\pi/2} T(n_{\text{env}}, n_{\text{housing}}, \theta_{\text{inc}}) \cdot T(n_{\text{housing}}, n_{\text{fill}}, \theta_j(\theta_{\text{inc}})) \\ &\cdot\ T(n_{\text{fill}}, n_{\text{tube}}, \theta_k(\theta_j)) \sin\theta_{\text{inc}}\, d\theta_{\text{inc}} \\ &\times \cos\theta_{\text{crit}}\end{aligned} \tag{6}$$

where $T(n_i, n_j, \theta_l)$ is the transmission probability at the interface between two media of refractive indices n_i and n_j for an incident angle θ_l determined by Snell's law on the previous layer. There is already an optimal value for the refractive index of the filling in this simplified approach. However, the radii of the cylinders have a non-negligible impact here because the curved pressure housing can have a focusing or defocusing effect in the transverse plane, and the inner tube could be missed altogether.

Therefore, in order to find the optimal refractive index of the filling material for the prototype geometry, the cylindrical geometry of the WOM is modeled in an MC simulation (in this ray-tracing algorithm, which was written in Python, photons start from a rectangular plane that is uniformly rotated around the WOM; the photons are propagated through the WOM surfaces, taking Fresnel losses and angular changes via Snell's law into account; the number of photons captured by total inner reflection are counted and divided by the total number of photons, as well as the area of the generation plane, to get the combined capture efficiency), propagating incident photons with Fresnel equations and Snell's law in three dimensions. The wavelength dependence of the refractive indices is negligible, and it is assumed that all refractive indices are fixed at a wavelength of $\lambda = 589\,\text{nm}$. The capture efficiency derived from this simulation is shown in Figure 5 and compared to the co-planar model. The optimal refractive index of the filling increases with larger refractive indices of the environment to a maximum at $n \approx 1.32$ with $\epsilon_{\text{comb}} = 38.3\%$ for water and ice. For water and ice, the filling could be ethanol or methanol, which have the disadvantage that they dissolve the WLS paint, or perfluoropolyether (PFPE), which is comparatively expensive.

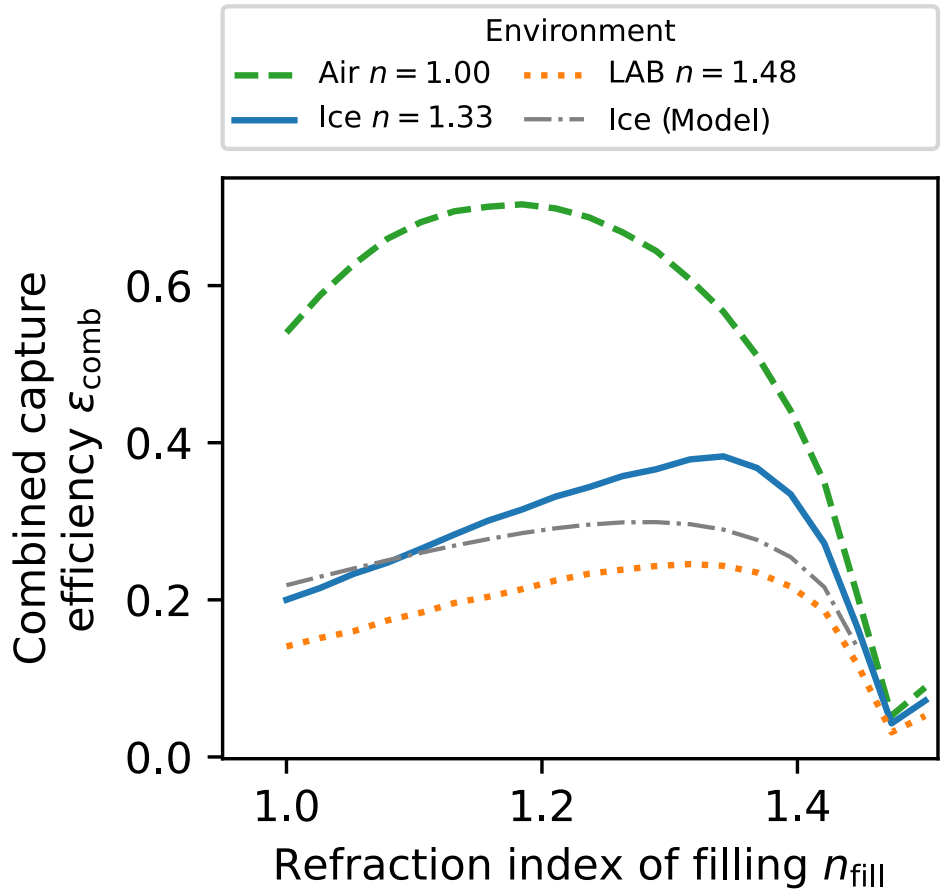

Figure 5. The combined efficiency for WOM operation in ice (or water), air, and LAB derived by simulating the propagation of 5×10^5 photons that are incident isotropically. The maximum achievable efficiency is 38.3% in ice at $n \approx 1.32$, 70.3% in air at $n \approx 1.18$, and 24.5% in LAB at $n \approx 1.32$ (refractive index for LAB taken from Ref. [9]). For the geometry, the prototype design is used, as specified in Section 1.

3. Coating

In addition to the optimization of the WOM design based on theoretical considerations, as presented in the previous section, some components are optimized empirically.

The absorption probability for photons incident on a WLS paint layer is given by

$$\begin{aligned} \epsilon_{\text{LY}}^{\text{WLS}} &= \left(1 - e^{-d \cdot \sigma_{\text{WLS}}(\lambda) \cdot n(c)}\right) \cdot \epsilon_{\text{QY}}^{\text{PL}} \\ &\simeq (1 - 10^{-\delta_{\text{OT}}}) \cdot \epsilon_{\text{QY}}^{\text{PL}} \\ &= (1 - e^{-d/\lambda_{\text{abs}}^{\text{inc}}}) \cdot \epsilon_{\text{QY}}^{\text{PL}} \end{aligned} \tag{7}$$

Here, d denotes the distance of a photon traveling inside the WLS matrix—i.e., the thickness of the coating—and $\sigma_{\text{WLS}}(\lambda)$ stands for the cross-section of the wavelength shifter with incident photons of wavelength λ. The number density of WLS particles along the incident photon path $n(c)$ solely depends on the concentration of WLS in the matrix c. The effectiveness of the light absorption can be expressed either in the form of an optical thickness $\delta_{\text{OT}}(\lambda)$ or in terms of an absorption length $\lambda_{\text{abs}}^{\text{inc}}(\lambda) = 1/(\sigma_{\text{WLS}}(\lambda) \cdot n)$. The emission efficiency of the WLS paint is denoted as $\epsilon_{\text{QY}}^{\text{PL}}$.

In this chapter, the steps taken along the development of the WLS coating are outlined, as are the considerations on the coupling of the tube and PMT. First, the test setup that was built to aid the optimization and to measure the WOM characteristics given in the next section is presented.

3.1. Test Stand

The scope of the test stand is to measure the local sensitivity of a WLS tube and its timing characteristics. The setup is schematically depicted in Figure 6. In the test stand, a Xenon arc lamp [15] serves as a light source for wavelengths between 250 nm to 700 nm. The lamp is coupled to a monochromator [16] of which the slit width is set in such a way that the bandwidth of the selected wavelength is $\sigma_\lambda = 1.06\,\text{nm}$.

The monochromatic beam is chopped to allow for a signal readout via a *lock-in* amplifier [17]. The chopper frequency is fed into two lock-in amplifiers, which demodulate a PMT signal. Subsequently, the light passes a diffusor, which shapes the beam to a homogeneous Gaussian profile. The beam is split up by a beam splitter. The reflected fraction of the beam illuminates a reference photodiode [18] to correct for lamp intensity variations, while the transmitted fraction is guided into a dark box to illuminate a WLS tube using a liquid light guide [19]. The end of the light guide in the dark box can be moved along the symmetry axis (the z_{Tube} position) and the azimuthal angle ϕ_{Tube} (note that this is a different definition from that of the variable ϕ in the flattened model in Equation (5)). The size of the illumination spot is around 1 cm in diameter. Thereby, selected points in ϕ_{Tube} and z_{Tube} on the tube surface can be illuminated to determine the local efficiency. The light is detected at both tube ends using PMTs [11]. The PMT surface is described in polar coordinates with the radius r and the angle ψ_{PMT}.

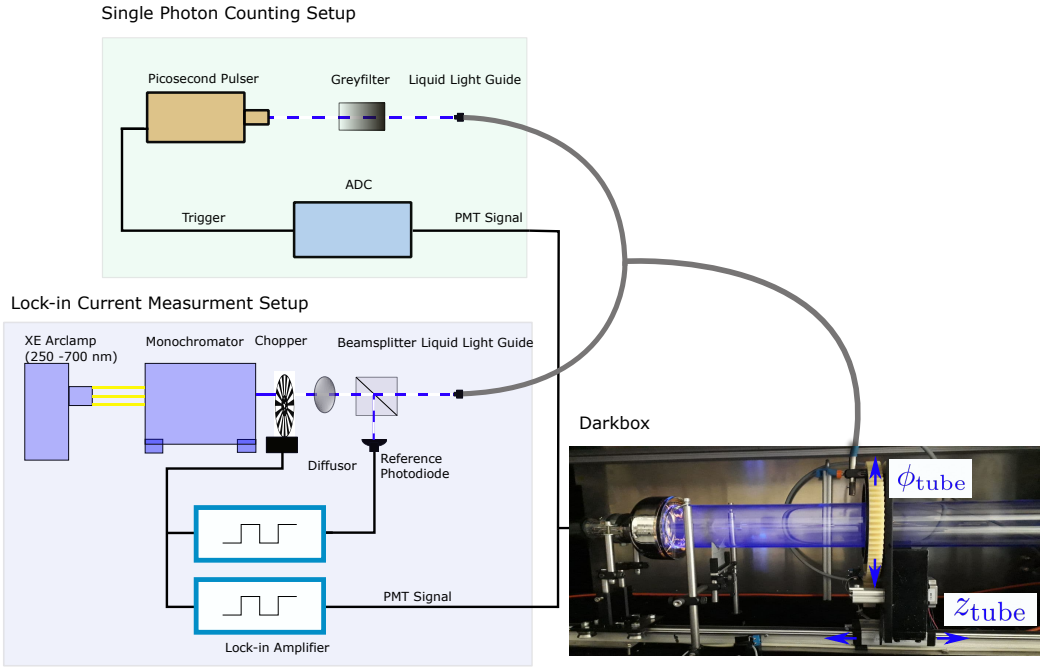

Figure 6. Schematic of the WOM test stand with a photograph of the darkbox.

In this *lock-in* setup, the efficiency of the WOM for a given light source position and incident wavelength is calculated as

$$\epsilon_{\text{lock-in}}(\lambda, \phi_{\text{Tube}}, z_{\text{Tube}}) = \frac{I_{\text{sig}}^{\text{corr}}(\lambda, \phi_{\text{Tube}}, z_{\text{Tube}})}{\frac{1}{N_{\text{steps}}} \sum_i I_{\text{ref}}^{\text{corr}}(\lambda, \psi_{\text{PMT,i}})} \tag{8}$$

Here, $I_{\text{sig}}^{\text{corr}}$ refers to the PMT output current corrected by the reference diode signal. For the reference measurement, the light source illuminates the PMT directly. The current $I_{\text{ref}}^{\text{corr}}$ is measured on the tube radius by varying ψ_{PMT} in a total of N_{steps} steps around the circumference; in our case, $N_{\text{steps}} = 36$. The mean of these measurements is calculated to take the PMT sensitivity variations on the photocathode into account. The resulting currents

of signal and the reference measurement are corrected for the wavelength-dependent quantum efficiency of the PMT, as well as for the intensity variations of the light source.

An overview of systematic uncertainties in the efficiency determination in the test stand is given in Ref. [20]. The largest uncertainty is the coupling of the WOM tube to the PMT using optical gel instead of a gel disc. An overall systematic error of approximately 4% in the efficiency determination for the prototype tube was obtained. This value was obtained by repeatedly coupling the tube and PMT with gel to measure the variance of the one-sided efficiency induced by the losses at the interface ϵ_{IF}. Additionally, the variation of the paint layer was taken into account (compare Figure 10). The values for the currents $I_{\mathrm{sig}}^{\mathrm{corr}}$ and $I_{\mathrm{ref}}^{\mathrm{corr}}$ are averaged over a time window of 2 s at a chopping frequency of 120 Hz, and the standard deviation is used as uncertainty.

The described setup can be adjusted for *single-photon* readout by replacing the Xe-Lamp, monochromator, and chopper with a 375 nm pico-second pulser [21]. The pulser is dimmed so that ∼6% of the waveforms recorded with a triggered fast ADC [22] include one photon signal within the expected time window. For the *single-photon* readout, the collection efficiency of the tube $\epsilon_{\mathrm{single}}$ is determined by the ratio:

$$\epsilon_{\mathrm{single}} = \frac{n_{\mathrm{sig}}(\lambda, \phi_{\mathrm{Tube}}, z_{\mathrm{Tube}}) - n_{\mathrm{bkg}}}{\frac{1}{\mathrm{N_{steps}}} \sum_i \left(n_{\mathrm{ref}}(\lambda, \psi_{\mathrm{PMT},i}) - n_{\mathrm{bkg}} \right)} \tag{9}$$

where n_{sig} denotes the number of photons detected when illuminating the point $(\phi_{\mathrm{Tube}}, z_{\mathrm{Tube}})$ with wavelength λ. The number of photons detected when directly illuminating the PMT is denoted by n_{ref}, and n_{bkg} is the number of photons falsely reconstructed from background light. The stability of the pulser was measured over a 12 h cycle, and the light output variance was found to be smaller than 2%, and was thus a subdominant contribution to the overall systematic error. The statistical error was calculated based on the number of measured photons n for each measurement. Since the same systematics as in the lock-in amplifier setup apply, the estimated systematic error for this setup amounts to approximately 4%.

3.2. Chemical Composition

Wavelength shifting is a special case of photofluorescence. The WLS molecules are excited when absorbing short-wavelength photons. After a decay time on the order of 1 ns to 2 ns [23] depending on the specific wavelength shifter, the molecule returns to the ground state, and a photon of a larger wavelength is emitted. A fraction of the energy is dissipated non-radiatively.

The WLS paint for the WOM is selected from a large number of variants with regard to the following criteria, as treated in detail in Ref. [24]:

- maximal overlap of the emission spectrum and the sensitivity of the readout PMT;
- large Stokes shift, i.e., minimal overlap of the absorption and emission spectra;
- maximal transparency of the WLS paint for re-emitted photons;
- similar refractive index of the coating and the WLS tube material;
- good adhesiveness and mechanical properties;
- optical thickness to enable reaching high concentration of WLS film to absorb 100% of the light for a broad spectrum.

The best results are obtained with a solution of toluene containing 213 g/L of the plastic polyethylmethylacrylate (PEMA) [25], which provides the matrix for the wavelength-shifting molecules, and a wavelength-shifting dye mix of 1.3 g/L Bis-MSB and 2.6 g/L p-Terphenyl per liter (the proportions given apply to the mixing process of the paint; in the paint layer of a coated tube, the proportions differ as the toluene evaporates during drying). The absorption spectrum of p-Terphenyl lies well below the Bis-MSB absorption spectrum. Since the emission spectrum of p-Terphenyl lies within the absorption spectrum of Bis-MSB, adding p-Terphenyl yields a sensitivity enhancement in the lower UV region.

3.3. Coating Process

For the tube material, PMMA (polymethylmethacrylate) and quartz glass are considered due to their optical properties with attenuation lengths for photons of multiple meters [14,26]. PMMA and PEMA are both soluble in toluene, which yields a transit region in which the two materials are mixed. This guaranties a strong bond that is able to withstand shearing forces generated by the different coefficients of thermal expansion over a wide temperature range. Since quartz glass is not soluble in toluene, the paint is bonded by van der Waals forces only.

Since the bond between quartz glass and the paint is purely of van der Waals nature, any contamination on the tube surface affects the bonding strength of the paint. When the tube surface is treated with a sequence of citric acid, acetone, and isopropanol, we find good adhesion in the subsequent coating. An alternative method is the usage of caustic soda and cleaning agent [27]. Both methods yield satisfying results. Current versions of coated quartz tubes have proven to be stable over time. We found no signs of delamination in several freezing cycles. Additionally, no significant deterioration of the paint layer when exposed to laboratory light was observed.

The coating can be applied to the inside or outside of the cylinder. It is also possible to coat both sides, but generally, high enough absorptivity for the incident UV light can be obtained with a single coating. Some major differences between in- and outside coating are summarized as follows:

- Coating on the inside shifts the light emission point towards the center, resulting in a reduced capture efficiency, as discussed in Section 2.1. The performance loss will increase with the thickness of the tube and the refractive index of the environment in which the coated tube is deployed.
- While quartz glass has high transmission down to wavelengths of 180 nm, PMMA is generally opaque to light below 300 nm [28], but in commercial products, it is often doped with additional UV absorbers to reduce aging in sunlight, thus limiting the UV light yield. Quartz glass can therefore be coated on either side, while PMMA performs best when coated outside.
- Coating a tube on the inside allows for easier handling. Impurities such as fat or dirt act as scattering centers for photons traveling inside the tube. Under UV light illumination, contaminated areas are clearly visible, presumably because photons couple out of the tube at these sites. The WLS paint is hydrophilic and therefore delaminates as a whole when immersed in water, rendering the tube opaque to light.
- In an assembly, an inside-coated tube will not interact chemically with the medium surrounding it, allowing for the surrounding medium to be chosen freely. While embedding the module in a housing can alleviate the problem in a similar way for outside-coated tubes, a filling material is generally required between the housing and the tube (see Figure 5), transferring the problem to chemical compatibility with the filling material.

In order to apply coatings to tubes, two simple techniques were developed, which are both based on the industrially employed *dip-coating* method [29,30]. For an external coating, the tube is vertically immersed in the paint and removed at a controlled speed to yield a homogeneous coating of adjustable thickness. Plugs are used to keep the inside of the tube paint free. In order to achieve an internal coating, the tube is filled completely with paint, which is then released at a constant flow rate using a valve. Due to the viscosity of the WLS solution, a higher velocity of extracting the paint in the coating process leads to a thicker paint layer (see Equation (10)). Both coating procedures are performed at a temperature of (20 ± 1) °C, and the tubes stay immersed in the paint for 90 s before the paint or tube is extracted at a fixed velocity. Both processes are operated in the Landau–Levich–Derjaguin (LLD) regime [31] where, for sufficiently high viscosity η and coating speed v_{coating}, the wet-film thickness is given as [29,30]

$$d_0 = 0.8 \cdot \sqrt{\frac{v_{\text{coating}}\eta}{\rho g}} \tag{10}$$

Here, ρ denotes the density of the paint and g is the gravitational acceleration. As the solvent evaporates, a dry film of constant thickness $d = \epsilon_d \cdot d_0$, with $\epsilon_d = \rho_{\text{PEMA}}/\rho_{\text{paint}} = 0.198$, is deployed on the surface. The relative factor ϵ_d corrects for the paint densities before and after coating. Aside from its simplicity, it is found that this method yields excellent surface quality. Using profilometer measurements on microscope slides coated with this technique, a small-scale surface roughness of <5 nm and a wavyness of 50–100 nm on scales of 10 µm was found; see Figure 7.

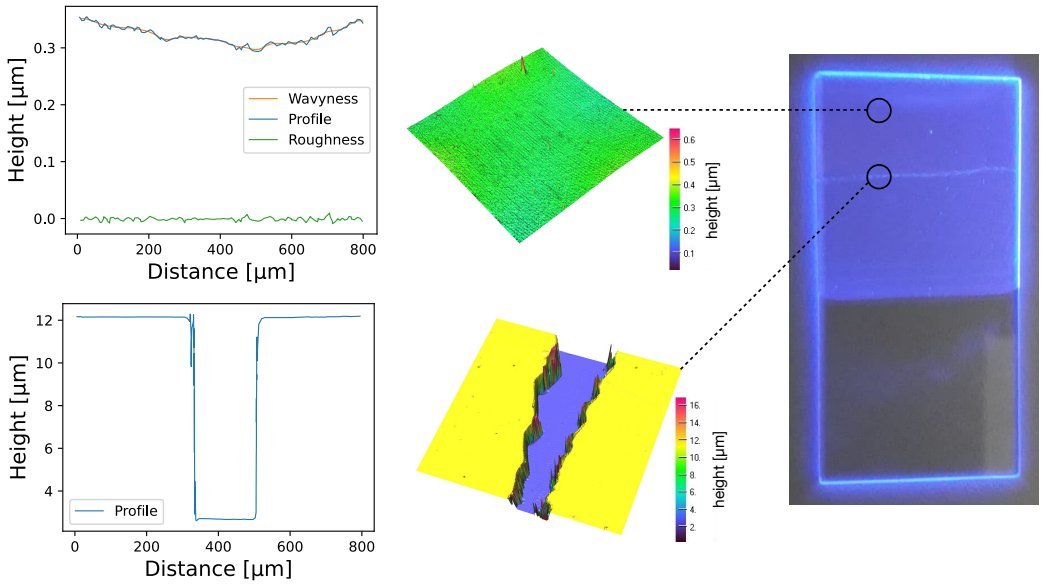

Figure 7. Profilometer measurements of two different paths on a slide coated with the wavelength shifter are shown. In each row, the measured profile is shown on the left, and a three-dimensional profile is shown in the middle. The path in the bottom row comprises a scratch in order to measure the thickness of the coating. A photograph of this slide is shown on the far right, in which the approximate measurement points are indicated.

In Figure 8, the effects of the variation of coating velocity v_{coating} and concentration of the wavelength shifter Bis-MBS $c_{\text{Bis-MBS}}$ on the absorption of the paint layer as a function of the wavelength are shown. To verify that the absorption efficiency follows Equation (7), we use the $\sigma_{\text{WLS}}(\lambda)$ dependency from the lowest absorption curve to estimate the optical depth for the other coating speeds and concentrations. The fit and data values are in good agreement. Comparing the different variations, it can be observed that high paint layer thicknesses lead to an overall broadening of the absorption spectrum up to a maximum where all incident photons are absorbed. In this way, the absorptive properties of the WLS paint can be optimized.

In Figure 9, the relative light yield of PMTs at the end faces of quartz and PMMA tubes coated on the outside is shown as a function of the coating velocity. The incident light has a wavelength of 375 nm. For quartz, the same tube was coated and measured, and the coating was removed again. This procedure was repeated at different velocities and twice for the highest velocity. For PMMA tubes, the coating could not be removed, so a different individual PMMA tube was coated for each measurement. As soon as nearly complete absorption of the injected light is achieved, a further increase in the coating thickness yields no further increase in efficiency. For the highest velocity, the two efficiencies obtained in the two coatings of quartz glass differ by significantly less than the measurement error, indicating that the coating process is well reproducible. In comparison, the results achieved for PMMA tubes show a larger spread and significantly lower efficiency values

(see Figure 9), indicating a less reliable coating process. The larger value simultaneously obtained for the absorption length for incident light $\lambda_{\text{abs}}^{\text{inc}}$ possibly suggests that the tube surface is partly dissolved by the toluene in the coating process, thus locally diluting the wavelength-shifter concentration.

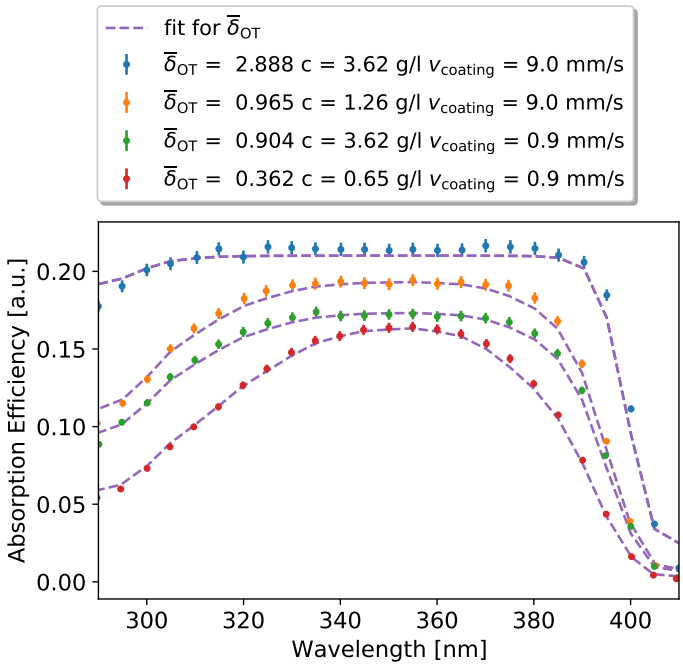

Figure 8. Absorption efficiency for different coating velocities v_{coating} and concentrations c of Bis-MSB in a WLS paint mixture of 400 mL of anisole and 85.1 g of PEMA (the second WLS was not used here). The methodology of the experiment is described in Ref. [24]. Shown in purple are fits to the different absorption efficiencies using Equation (7) multiplied by a normalization constant.

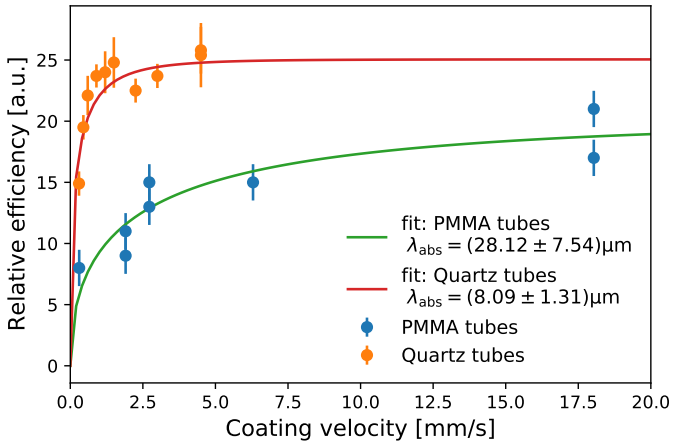

Figure 9. One-sided efficiency at 375 nm versus the coating speed for quartz tubes and PMMA tubes. Efficiencies are read out by a PMT 150 mm away from the illumination point. The solid lines show a fit with the thickness and absorption model from Equations (7) and (10).

The obtained absorption length $\lambda_{\text{abs}}^{\text{inc}}$ for quartz can be transformed into an optical depth using Equation (7) and the estimated paint thickness of 2 $\times$17 µm (paint layers on both sides of the tube contribute) to be $\delta_{\text{OT}} = 1.83 \pm 0.30$. This number lies well within the different optical thicknesses obtained in Figure 8.

In Figure 10, a measured relative efficiency over half the surface of a quartz tube is shown. The current $I_{\text{sig}}(z, \phi)$ is measured in steps of 10° in azimuth angle ϕ and 10 mm

in a cylinder of height z. The intensity value at a given position z is divided by the corresponding value at $\phi = 0$. In conclusion, an overall relative variation of the paint layer efficiency of $\pm 5\%$ was obtained.

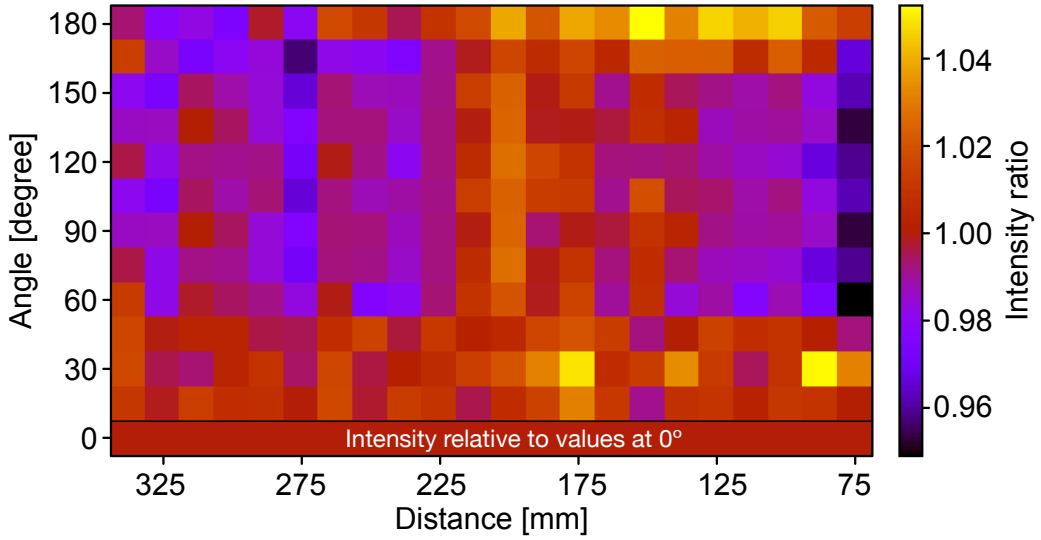

Figure 10. A 2D scan of the relative efficiency of a quartz tube. For a given longitudinal position, the efficiency is relative to the corresponding value at 0° in order to correct for the longitudinal intensity dependence. The angular variation of the efficiency is less than $\pm 5\%$.

3.4. Absorption and Emission

In order to measure the properties of the WLS coating, quartz microscope slides were coated with a thin film of WLS paint. The coated slides were then illuminated by a 365 nm UV LED focused on the paint layer. The angular distribution of the emission was measured in the UV band ($\lambda = 365 \pm 10$ nm) to test for complete absorption of the UV light, as well as in the optical range ($\lambda = 450 \pm 40$ nm) to investigate the re-emission. In Figure 11, the measured absorption and emission spectra of the WLS paint are shown together with an absorption measurement of a fully coated quartz tube.

Between 280 and 400 nm, the paint is around 92.7% absorptive for a sufficiently thick paint layer. The overlap between the absorption and emission spectra is a small band between 400 nm to 420 nm. Therefore, by calculating the overlap, a re-emission and consecutive capture probability of 99.61% is expected in air. The emission spectrum peaks around 440 nm, which is the high-quantum-efficiency region for standard PMTs that have a borosilicate window and a bialkali photocathode.

3.5. Deterioration

The setup described in Section 3.4 was further used to explore possible deterioration of the paint layer due to high UV exposure. It was found that focusing the light output of the diode with 100 mW on a spot size of 1 mm^2 over several hours led to a deterioration of the paint layer. A diffuse illumination of the entire slide with 1250 mm^2 using the same light intensity showed no damaging effects on a time scale of days. In conclusion, with a damage threshold on the order of $mW/mm^2 \times h$ deterioration of the paint due to illumination is not a limiting factor. The UV light intensity in detector experiments in which the WOM is a suitable light sensor will be orders of magnitude lower.

Degradation of efficiency was not found either with time or after exposing the tubes to cold temperatures.

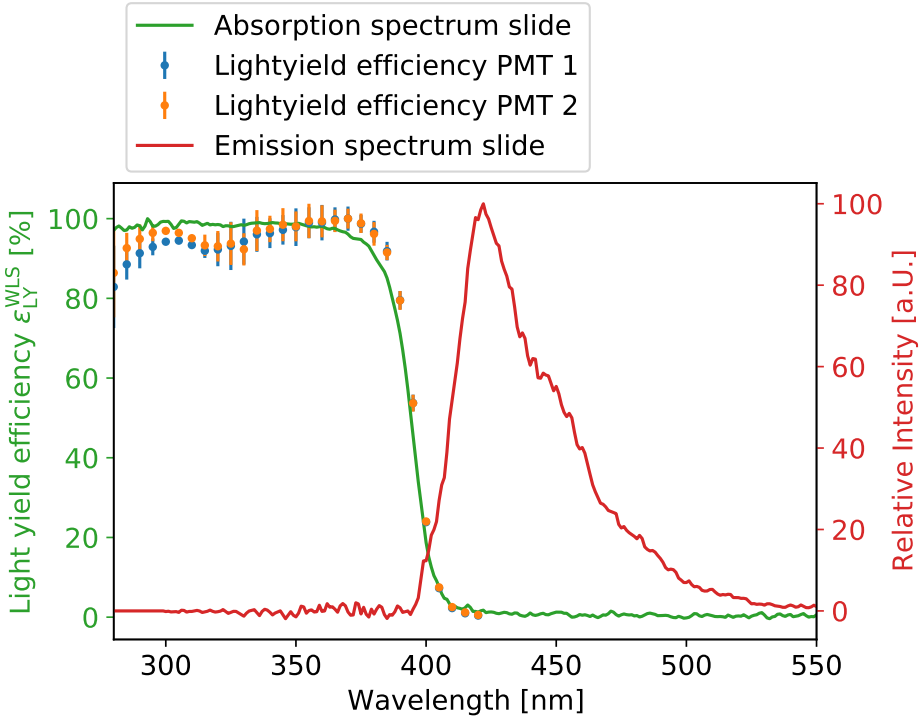

Figure 11. Absorption (green) and emission spectra (red) of a WLS-coated quartz slide. The light yield efficiency ϵ_{LY}^{WLS} measured on the prototype tube is shown in blue and orange. The methodologies of the experiments are described in Refs. [24,32].

3.6. Optical Coupling

In order to minimize photon losses at the interface between the end face of the WOM tube and PMT glass, different methods of optically coupling the two components were used. For repeatability of different experiments, an optical coupling gel [12] was used in most experiments. However, for a deployable WOM, where a disassembly of the module is not desired, optical glue [33] is the preferred choice. The refractive index of the cured glue was chosen to lie between quartz glass ($n = 1.46$) and borosilicate glass ($n = 1.51$, used for the PMT surface) to minimize Fresnel losses at the interface. It should be noted that flat-surface PMTs are preferable when using optical glue, since spherical PMTs require chamfered ends of the WLS tubes to fit the curvature of the PMT perfectly. If this is not the case, cracks in the glue layer are observed, which likely reduce bond strength and transmission efficiency of the glue. Given the transmission from the datasheet and the Fresnel losses at the interface (calculated using the angular distribution of the light output of the WOM from simulation), a transmission probability of $\epsilon_{IF} > 90\%$ is expected when using optical glue for the coupling.

It would be desirable to concentrate the light emission of the WOM from the tube cross-section onto a compact area, allowing one to further reduce the photocathode area of the readout PMT. While conservation of etendue does not prohibit this if the cross-sectional area is preserved, a viable solution was not found. Starting from theoretical calculations [34], several approaches have been investigated in simulations [13,35] and experiments [36]. It was found that all lead to severe efficiency losses (in simulation, this is mostly due to photons being reflected back into the tube) and are therefore not suitable for the WOM design.

4. Characterization

In order to compare the WOM with other light sensors, measurements of its characteristics were conducted, i.e., the one-sided efficiency $\epsilon_{\mathrm{one-sided}}$ (see Equation (5)), the transit

time spread, and the dark noise. The effective area and the signal-to-noise ratio (SNR) were derived from these values, as well as the efficiencies discussed in the previous sections.

4.1. Efficiency

In the absence of light reflected from the other end of the tube, the efficiency measured with the test stand described in Section 3.1 can be be identified with the one-sided efficiency in Equation (5). The efficiency of the WOM as a function of the z-position is determined using the *lock-in* setup (Equation (8)) and the *single-photon* setup (Equation (9)) independently for the same WLS tube. The results of both measurements overlap within their respective uncertainties. In Figure 12, the measured efficiency is shown as a function of the cylinder height z obtained for the 700 mm long, 60 mm outer diameter prototype quartz tube described in Section 1. The tube was coated on the inside at a speed of 25 mm s^{-1}. Using the obtained efficiency as a function of the distance z, the *flattened model* (see Section 2.2) was used as a fit function in conjunction with a normalization constant N as an additional fit parameter. The constant N accounts for light losses independently of the position along the tube z.

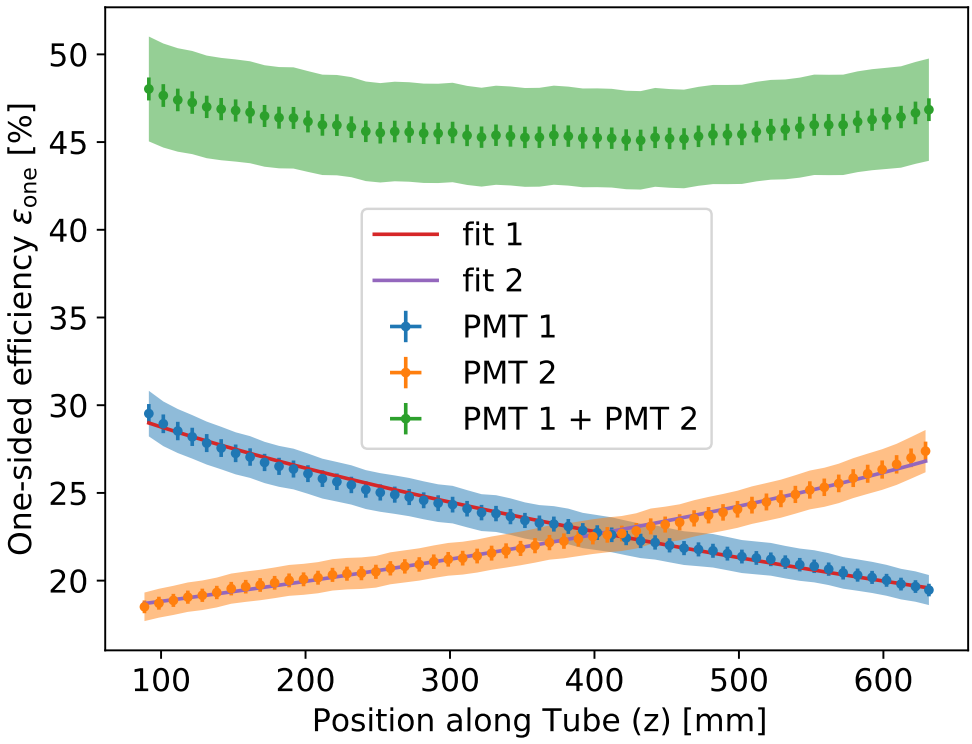

Figure 12. Efficiency as a function of the distance from the ends of the tube for a quartz tube [10]. The flattened model efficiency is used as a fit function to extract attenuation lengths. The injected light has a wavelength of (375.00 ± 1.06) nm. Systematic errors are shown as shaded areas.

The respective fits lead to attenuation lengths of (2851 ± 55) mm and (3233 ± 37) mm and normalization constants of (89.0 ± 0.4) % and (81.0 ± 0.2) %. The mean and standard deviation obtained for each PMT measurement result in an attenuation length of $\lambda_{att} = (3041 \pm 191)$ mm and a normalization constant of $N = (84 \pm 4)$%. Several factors contribute to the deviation of N from unity:

- Overlap between absorption and emission spectra of the WLS paint leads to reabsorption of emitted photons with an estimated 0.39% relative efficiency loss.
- Some efficiency is lost due to the inside coating of the tube (see Equation (4) and Figure 4). For the prototype, a reduction in capture efficiency ϵ_{TIR} compared to the outside coating of 4.2% is obtained.

- Interface losses are calculated using the difference in refractive indices between the tube ($n_{\text{Tube}} = 1.46$) and glass of the PMT ($n_{\text{PMT}} = 1.51$) together with the angular distribution on the end faces from the simulation. Averaging between s- and p-polarized transmission yields a relative loss of $1 - \epsilon_{\text{IF}} = 5.5\%$.

Concluding, aside from the aspects discussed here, only minor additional efficiency losses may occur, and in air, $\epsilon^{\text{meas}}_{\text{one-sided}} = (46.4 \pm 4.4)\%$ of photons can reach the end of the prototype tube.

4.2. Transit Time Spread of Photons

Using the *single-photon* setup described in Section 3.1, the transit time spread of photon coupling into the WLS tube is measured as a function of the distance to the PMT z. Here, the arrival time of each individual photon is calculated as the first bin in which the recorded waveform amplitude reaches half of the peak amplitude in the photon event (*constant fraction discriminator*). The transit time spread is the distribution of the individual arrival times. Measurements were taken on a 900 mm long outside-coated PMMA tube in increasing distance between the PMT and light entry point. The light pulser [21] had a full width at half maximum (FWHM) of $\sigma = 0.66$ ns, and the sampling time step of the ADC digitizing the PMT output was 1 ns. The time resolution of the WOM is a convolution of three effects [37]:

- Time resolution of the PMT, which is measured to be a Gaussian profile with $\sigma \sim 6$ ns.
- Absorption and re-emission of the WLS paint measured to be an exponential decay with $\tau \approx 1.5$ ns (in accordance with Ref. [23]). For the lower UV < 280 nm, where the light needs to be absorbed and shifted by p-Terphenyl first (as mentioned in Section 3), an additional exponential decay with a time constant of around 1 ns is expected.
- Photon trajectory path length distribution inside the tube depending on the absorption length of the material.

The final result, together with the FWHM of the distribution, is shown in Figure 13. The transit time spread of the full module has an FWHM of approximately $\sim$18 ns (a fit with a symmetric Gaussian gives σ =13.5 ns). The dominant contribution is caused by the photon propagation in the tube. A trend towards larger time delays for increasing distances z between PMT and the light entry point for the baseline response time can be observed.

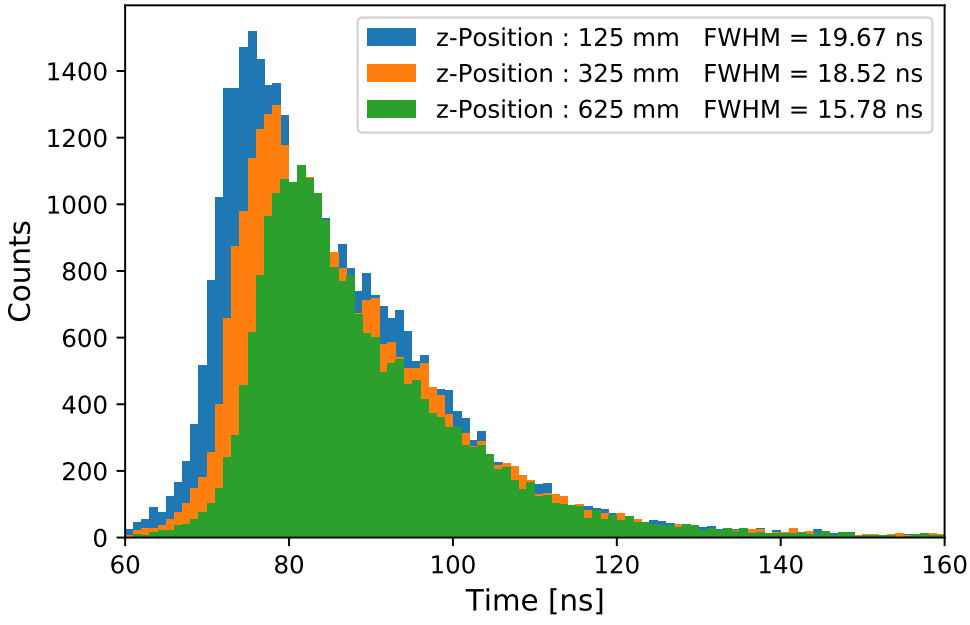

Figure 13. The measured transit time spread of a WOM tube with one attached PMT is shown for different z-positions along the tube.

4.3. Noise

The background noise of the WOM comprises the dark noise of the PMT and the scintillation noise caused by radioactive decays in the tube glass and, optionally, the glass of the housing. A climate chamber was used to measure the PMTs' dark noise rate at different temperatures. The PMTs were wrapped in black cloth and enclosed in a metal box to prevent impact from background light and radio frequency interference (RFI). To estimate the noise rate of the PMTs, a single photo-electron (SPE) spectrum was obtained from a measurement over time. An exponential together with a Gaussian was fitted to the data, and the number of photons under the Gaussian distribution was taken. The noise rate was then estimated by dividing the number of photons by the dead-time-corrected measurement length in seconds. The chosen PMTs had dark noise rates at -10 °C of $r_{\mathrm{DNR}}^{-10^\circ} = (172.5 \pm 27.7)$ Hz.

For the choice of the pressure vessel, quartz glass samples from different companies were tested. For the quartz glass of the prototype [10], a dark noise rate of $6\,\mathrm{Hz\,kg^{-1}}$ was measured at room temperature; thus, $r_{\mathrm{Tube}} = 4$ Hz for the 700 g tube and $r_{\mathrm{Housing}} = 50$ Hz for the 8.3 kg housing in the prototype design.

4.4. Effective Area

The mean projected effective area is defined here by

$$\left\langle A_{\mathrm{eff}}^{\mathrm{proj}}(\theta,\phi)\right\rangle = \frac{N_{\mathrm{det}}}{N_{\mathrm{sim}}^{\mathrm{plane}}} \tag{11}$$

where $N_{\mathrm{sim}}^{\mathrm{plane}}$ photons are emitted from a plane that is uniformly rotated around the detection device, and of these, N_{det} will be recorded by the device.

The effective area of a single PMT with a diameter of 3.5 inch (see Ref. [11]) is obtained by deriving the sensitive projected area for isotropic illumination using the MC simulation described in Section 2.3. Using a quantum efficiency of 18% averaged over the WLS emission wavelengths (400 nm to 500 nm) and cathode area, the effective area is approximately $A_{\mathrm{eff}}^{\mathrm{PMT}} = 12.0\,\mathrm{cm}^2$ in water, ice, or air as environment.

For a WOM in the prototype geometry (see Section 1), all losses from optical propagation into and in the WOM tube, as summarized in Equation (1), are multiplied by the projected sensitive area. The WLS efficiency is taken from the slide measurement in Figure 11. The fraction of captured photons $\varepsilon_{\mathrm{TIR}}$ is derived using Equation (3). The attenuation during propagation in the tube ϵ_{TP} in dependence on the distance to the tube end is taken from the data shown in Figure 12, where the TIR effect is factored out. The PMT efficiency is chosen as above, and the loss at the tube to glue or at the gel to PMT interfaces is chosen to be $\epsilon_{\mathrm{IF}} = 0.95$ (compare with Section 3.6). Then, the effective area of the WOM is approximately $A_{\mathrm{eff}}^{\mathrm{ice}} = 78.6\,\mathrm{cm}^2$ in water or ice and $A_{\mathrm{eff}}^{\mathrm{air}} = 126.4\,\mathrm{cm}^2$ in air, averaged over the wavelength range of 250 nm to 600 nm.

In the evaluated design, the effective area of the WOM exceeds the effective area of the single PMT by a factor of approximately $R_{\mathrm{ice}} = 6.5$ in ice and $R_{\mathrm{air}} = 11.3$ in air. The wavelength-dependent effective area of the WOM and a single PMT is shown in Figure 14. The Cherenkov spectrum (without attenuation in medium) is shown in parallel to illustrate the advantage of an enhanced sensitivity at a lower wavelength. The ratio of the average effective area improves to a factor of approximately $R_{\mathrm{ice}}^{\mathrm{Cher}} = 10.4$ in ice and $R_{\mathrm{air}}^{\mathrm{Cher}} = 18.9$ when weighted with the Cherenkov spectrum.

The effective area scales linearly with the diameter of the tube. The scaling of the effective area in dependence on the WOM length saturates due to the attenuation of photons during propagation in the tube, as shown in Figure 15. In reality, the dimensions are further restricted by several limitations: The dip-coating station would need to be scaled; glass tubes of appropriate quality are limited in diameter due to manufacturability; the high weight and bulkiness of the device complicate handling in the laboratory and during deployment.

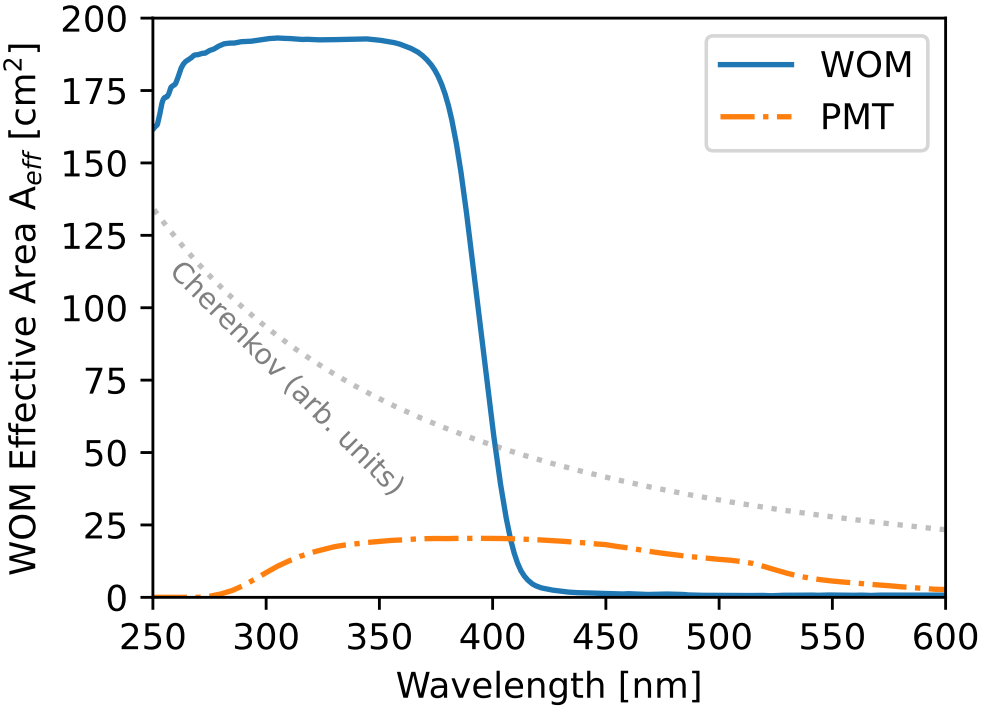

Figure 14. Effective areas of the WOM in the prototype design and a single PMT of this ensemble in dependence on wavelength estimated with the MC simulation described in Section 2.3, assuming both devices are deployed in ice.

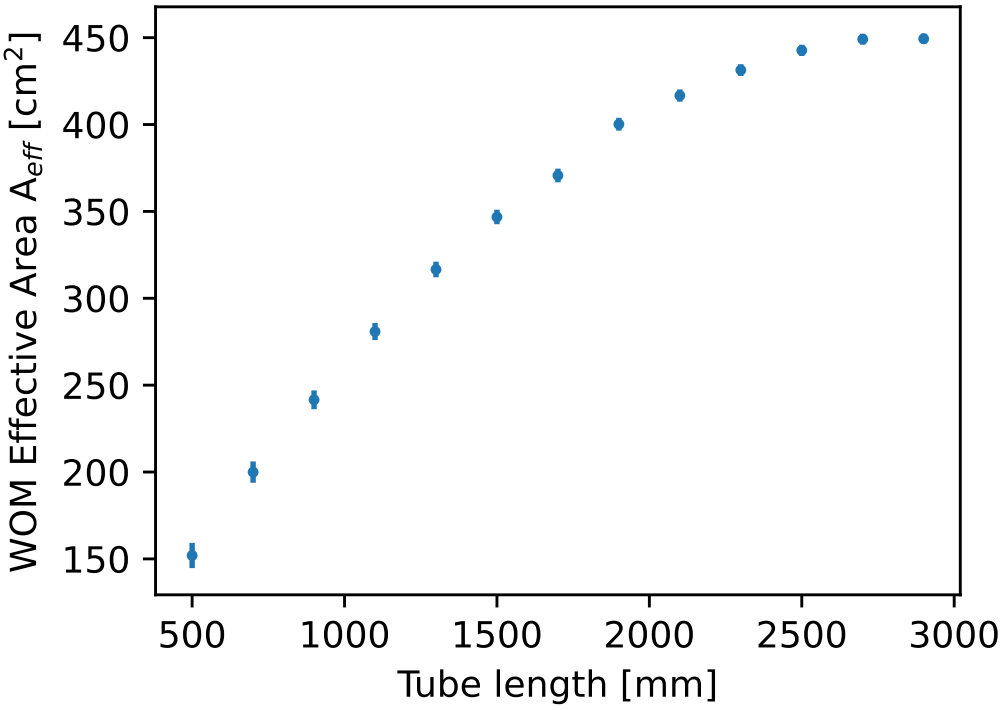

Figure 15. Scale of the effective area at low wavelengths in ice in dependence on the WOM tube length obtained by the MC simulation. Prototype specifications were used for all other properties of the WOM.

4.5. Signal-to-Noise Ratio

In order to calculate the signal-to-noise ratio (SNR) of the WOM in comparison to a single PMT, the averaged effective area from Section 4.4 is used as signal strength, and the sum of the noise measurement in Section 4.3 of all components is used for the denominator. In practice, the noise of the WOM components would not sum up, at least not for bright signals, because one would add a coincidence requirement for photons hitting both PMTs, which should reduce the noise significantly. Here, noise rates are summed up conservatively.

For the WOM SNR, this calculation yields improvement factors of approximately $F_{\text{ice}} = 3.2$ or $F_{\text{air}} = 5.5$ compared to a single PMT embedded in ice or air. Weighting the effective area with a Cherenkov spectrum (without photon attenuation in medium) would improve the SNR even further. The corresponding improvement factors are approximately $F_{\text{ice}}^{\text{Cher}} = 5.2$ in ice and $F_{\text{air}}^{\text{Cher}} = 8.9$ in air.

5. Conclusions, Applications, and Outlook

In this work, a novel photosensor concept is described in which PMTs are complemented with a tube with wavelength-shifting coating in order to enhance the signal-to-noise ratio. It is demonstrated that consistent coatings can be applied in a simple procedure to glass tubes, which allows one to effectively convert the UV fraction of the incident spectrum. Theoretical studies and experimental work were conducted to understand all features of this concept and its performance in detail. In particular, it is shown that, in air, $\epsilon_{\text{one-sided}}^{\text{meas}} = (46.4 \pm 4.4)\%$ of the converted photons can be detected at the end of the prototype tube. This simple concept can thus be applied to significantly enhance the light collection area of any light sensors. As the WLS tube does not add significantly to the dark noise, for the prototype design, this leads to improvement factors in the Cherenkov weighted signal-to-noise ratio of $F_{\text{air}}^{\text{Cher}} = 5.2$ in ice and $F_{\text{ice}}^{\text{Cher}} = 8.9$ in air. As a side effect, the sensitivity of the WOMs is improved in the UV, which is particularly beneficial for the detection of Cherenkov or scintillation light by matching the emission spectrum of the WLS paint with the PMT wavelength sensitivity. Aside from the PMT, the cost of the module is dominated by the coated glass tube, while expenses of the paint and glue are insignificant due to the small amounts required for each module. The transit time spread of detected photons is wider than for bare PMTs because it is smeared predominantly by the propagation time in the tube. While the photosensors at the tube ends can be read out independently, only a single photon is generated in the wavelength-shifting process, so in single-photon detection mode, no information about the incidence position along the tube can be obtained.

The prototype design does not reach the maximal sensitivity possible in an optimized geometry due to practical considerations. A wider and longer tube, if manageable, would improve the SNR. Silicone photomultipliers (SiPMs) could be chosen for the tube readout in bright conditions, e.g., when deploying in liquid scintillator as a detector medium. Light guides were evaluated to couple smaller PMTs to wider tubes. However, this has stringent theoretical limitations and proved complicated in practice.

One prototype module enclosed with a vessel was built using simple *off-the-shelf* electronics as *proof of concept* following the prototype design described in this work; see Figure 16. Hydrogel [38] was used as a filling material to improve the optical properties of the module. The module was deployed in the Canadian sea at a depth of 2539 m within the Ocean Network Canada [39]. It operated stably at the given conditions and provided data on the local bio-luminescence.

Another application for which prototypes are already at hand is the envisioned SHiP experiment [40,41]. SiPMs are coupled to the WLS tubes, which are to be deployed in the veto chamber of the experiment.

For the upcoming IceCube Upgrade, which extends the low-energy infill of IceCube, a WOM with an improved design that has been adjusted to the environmental needs has

been designed. Twelve modules with 1300 mm long pressure vessels, 5-inch PMTs, and customized electronics have been developed and will be deployed [42].

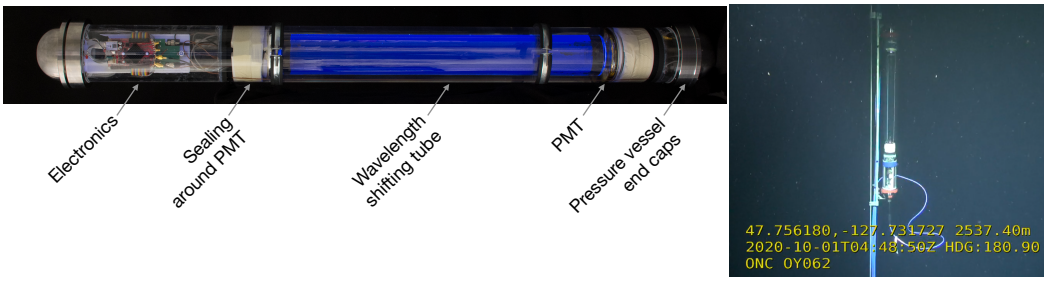

Figure 16. A demonstrator device made in the prototype configuration and photographed under UV illumination (**left**). The electronics comprise a PMT pulse readout, environmental sensors, and communication. After deployment, a photograph was taken by a robot in the Ocean Network Canada. (**right**). Right picture: Courtesy of the ONC.

Author Contributions: Investigation and methodology: B.B.-Q., L.S.B., S.B., J.B.-K., D.H., K.H., T.K., L.K., M.K., P.P., A.P., J.R.-H., M.R., L.S., F.T. and A.V.; Supervision: S.B., K.H., T.K., L.K. and M.K.; Writing—review and editing: S.B., A.P. and J.R.-H. All authors have read and agreed to the published version of the manuscript.

Funding: We acknowledge the support from the following agencies: Bundesministerium für Bildung und Forschung (BMBF), Deutsche Forschungsgemeinschaft (DFG) in particular through the clusters of Excellence PRISMA and PRISMA+, Initiative and Networking Fund of the Helmholtz Association, Deutsches Elektronen-Synchrotron DESY. We acknowledge support from the Open Access Publication Fund of the University of Wuppertal.

Institutional Review Board Statement: Not applicable.

Informed Consent Statement: Not applicable.

Acknowledgments: We acknowledge the fruitful discussion with all of the individuals involved in establishing the WOM as a sensor for the SHiP surround background tagger (SBT). We are very grateful to the ONC and the P-ONE Collaboration for the deployment of the WOM prototype as part of the STRAW-b installation. We would also like to thank Andreas Best from the Max-Planck-Institute for polymer research for the profilometer measurements, which allowed us to estimate the thickness of our WLS coatings. We are thankful to Jochen Schreiner and Hardy Simgen of the Max-Planck-Institute for Nuclear physics in Heidelberg, as well as Christoph Düllmann from the Institute of Nuclear Physics in Mainz for the radioactive impurity measurements on our glass samples. We further acknowledge the numerous studies conducted by students in the context of the WOM that are not explicitly presented in this publication. In particular, these are: Kristina Sand [2], Peter Falke [1], Carl Fösig [2], Esther del Pino Rosendo [2], Jan Weldert [2], Elisa Lohfink [2], Christian Matthe [2], Lucas Binn [2], Sandra Gerlach [2], Alexandre Portier [4], Yuriy Popovych [2], Daniel Popper [2], Ronja Schnur [2], Andreas Looft [3], Jakob Beise [3], Maximillian Bubeck [2], Maximillian Thiel [2] , Nich Jannis Schmeisser [5] from the institutions: [1] Universtität Bonn, [2] University of Mainz, [3] DESY , [4] PHELMA Grenoble, [5] University of Wuppertal.

Conflicts of Interest: The authors declare no conflict of interest.

References

1. Aartsen, M.G.; Ackermann, M.; Adams, J.; Aguilar, J.A.; Ahlers, M.; Ahrens, M.; Altmann. D.; Andeen, K.; Anderson, T.; Ansseau, I.; et al. The IceCube Neutrino Observatory: Instrumentation and Online Systems. *JINST* **2017**, *12*, P03012. [CrossRef]
2. Fukuda, S.; Hayato, Y.; Iida, T.; Iyogi, K.; Kameda, J.; Kishimoto, Y.; Koshio, Y.; Marti, L.; Miura, M.; Moriyama, S.; et al. The Super-Kamiokande detector. *Nucl. Instrum. Meth. A* **2003**, *501*, 418–462. [CrossRef]
3. Alimonti, G.; Arpesella. C.; Back, H.; Balata, M.; Bartolomei, D.; de Bellefon, A.; Bellini, G.; Benziger, J.; Bevilacqua, A.; Bondi, D.; et al. The Borexino detector at the Laboratori Nazionali del Gran Sasso. *Nucl. Instrum. Meth. A* **2009**, *600*, 568–593. [CrossRef]
4. Boger, J.; Hahn, R.L.; Rowley, J.K.; Carter, A.L.; Hollebone, B.; Kessler, D.; Blevis, I.; Dalnoki-Veress, F.; DeKok, A.; Farine, J.; et al. The Sudbury neutrino observatory. *Nucl. Instrum. Meth. A* **2000**, *449*, 172–207. [CrossRef]

5. An, F.; An, G.; An, Q.; Antonelli, V.; Baussan, E.; Beacom, J.; Bezrukov, L.; Blyth, S.; Brugnera, R.; Avanzini, M.B.; et al. Neutrino physics with JUNO. *J. Phys. G Nucl. Part. Phys.* **2016**, *43*, 030401. [CrossRef]
6. Aprile, E.; Arisaka, K.; Arneodo, F.; Askin, A.; Baudis, L.; Behrens, A.; Brown, E.; Cardoso, J.M.R.; Choi, B.; Cline, D.; et al. The XENON100 dark matter experiment. *Astropart. Phys.* **2012**, *35*, 573–590. [CrossRef]
7. Akerib, D.S.; Bai, X.; Bedikian, S.; Bernard, E.; Bernstein, A.; Bolozdynya, A.; Bradley, A.; Byram, D.; Cahn, S.B.; Camp, C.; et al. The Large Underground Xenon (LUX) experiment. *Nucl. Instrum. Meth. A* **2013**, *704*, 111–126. [CrossRef]
8. Aalbers, J.; Agostini, F.; Alfonsi, M.; Amaro, F.D.; Amsler, C.; Aprile, E.; Arazi, L.; Arneodo, F.; Barrow, P.; Baudis, L.; et al. DARWIN: Towards the ultimate dark matter detector. *J. Cosmol. Astropart. Phys.* **2016**, *2016*, 017. [CrossRef]
9. Tseung, H.W.C.; Tolich, N. Ellipsometric measurements of the refractive indices of linear alkylbenzene and EJ-301 scintillators from 210 to 1000 nm. *Phys. Scr.* **2011**, *84*, 035701. [CrossRef]
10. Heraeus. HSQ 300. 2021. Available online: https://www.heraeus.com/media/media/hca/doc_hca/products_and_solutions_8/solids/Solids_HSQ300_330MF_EN.pdf (accessed on 26 January 2022).
11. Hamamatsu. R14689. 2021. Available online: https://www.hamamatsu.com/eu/en/product/type/R14689/index.html (accessed on 26 January 2022).
12. Eljen Technology. EJ-550. 2021. Available online: https://eljentechnology.com/products/accessories/ej-550-ej-552 (accessed on 26 January 2022).
13. Thomas, F. Light Propagation Simulation for the Wavelength-Shifting Optical Module on CUDA GPUs. Master's Thesis, Johannes Gutenberg University Mainz, Mainz, Germany, 2019. Available online: https://butler.physik.uni-mainz.de/icecube/thesis/master_Florian_Thomas.pdf (accessed on 26 January 2022).
14. Heraeus. Transmission Calculator for Optical Applications. 2021. Available online: https://www.heraeus.com/en/hca/fused_silica_quartz_knowledge_base_1/t_calc_1/transmission_calc_opt/transmission_calculator_opt.html?chartIndex=2&selection=suprasil_311_312%2Csuprasil_1_2a%2Csuprasil_2b%2Cspectrosil_2000&thickness=10&rangeX=120%2C4500 (accessed on 26 January 2022).
15. Quantum Design. Arc Light Sources 50–150 W Arc Light Source. 2022. Available online: https://qd-europe.com/fileadmin/Mediapool/products/lightsources/en/LQ_50_150_w_arc_light_source_en.pdf (accessed on 26 January 2022).
16. Quantum Design. Monochromators Monochromator MSH-300 with Variable Slit. 2022. Available online: https://qd-europe.com/fileadmin/Mediapool/products/Bentham/_pdf/MSH_300_with_variable_slit.pdf (accessed on 26 January 2022).
17. Zurich Instruments. zi MFLI Lock in Amplifier. 2021. Available online: https://www.zhinst.com/sites/default/files/documents/2021-12/zi_mfli_leaflet_v2.pdf (accessed on 26 January 2022).
18. Hamamatsu Photonics. Si Photodiodes with BNC Connector. 2022. Available online: https://www.hamamatsu.com/resources/pdf/ssd/s2281_series_kspd1044e.pdf (accessed on 26 January 2022).
19. Thorlabs. Thorlabs Liquid Light Guide. 2021. Available online: https://www.thorlabs.com/drawings/fe93bd8d318e7307-7BA1AD90-E649-0882-7162D968CDA653D9/LLG5-4T-SpecSheet.pdf (accessed on 26 January 2022).
20. Rack-Helleis, J. Efficiency Determination of the Wavelength-Shifting Optical Module (WOM). Master's Thesis, Johannes Gutenberg University Mainz, Mainz, Germany, 2019. Available online: https://butler.physik.uni-mainz.de/icecube/thesis/master_John_Rack-Helleis.pdf (accessed on 26 January 2022).
21. Rongen, M.; Schaufel, M. Design and evaluation of a versatile picosecond light pulser. *JINST* **2018**, *13*, P06002. [CrossRef]
22. Teledyne. SP Devices ADQ 14. 2021. Available online: https://www.spdevices.com/documents/datasheets/19-adq14-datasheet/file (accessed on 26 January 2022).
23. Kuzniak, M.; Szelc, A.M. Wavelength Shifters for Applications in Liquid Argon Detectors. *Instruments* **2020**, *5*, 4. [CrossRef]
24. Hebecker, D. Developement of a Single Photon Detector with Wavelength Shifting and Light Guiding Technology. Master's Thesis, University of Bonn, Bonn, Germany, 2014. Available online: https://www-zeuthen.desy.de/~hebecked/Publications_etc./Master_Thesis/Dustin_hebecker_master_thesis.pdf (accessed on 26 January 2022).
25. Preservation Equipment. Paraloid B72. 2021. Available online: https://www.preservationequipment.com/files//4ba8f3dc-85c1-44e4-9237-a3db00db1ef4/Paraloid%20B72%20Use.pdf (accessed on 26 January 2022).
26. Beise, J. Transport Losses in Light Guides for the WOM Application. Bachelor's Thesis, Humboldt-University Berlin, Berlin, Germany, 2019.
27. Carl Roth GmbH + Co. KG. Mucasol Universalreiniger. 2021. Available online: https://www.carlroth.com/de/de/reinigungsmittel-fuer-ultraschallgeraete/universalreiniger-mucasol/p/1a3l.1 (accessed on 26 January 2022).
28. Abdel-Mottaleb, M.S.; Ahmed, R.M. Optical Study on Polymethyl methacrylate/Polyvinyl acetate Blends. *Int. J. Photoenergy* **2009**, *2009*, 150389. [CrossRef]
29. Brinker, C.J. Dip Coating. In *Chemical Solution Deposition of Functional Oxide Thin Films*; Springer: Berlin/Heidelberg, Germany, 2013; pp. 233–261. [CrossRef]
30. Rio, E.; Boulogne, F. Withdrawing a solid from a bath: How much liquid is coated? *Adv. Colloid Interface Sci.* **2017**, *247*, 100–114. [CrossRef] [PubMed]
31. Derjaguin, B. On the thickness of the liquid film adhering to the walls of a vessel after emptying. *Prog. Surf. Sci.* **1993**, *43*, 134–137. [CrossRef]

32. Binn, L.S. Charakterisierung von dünnen Wellenlängenschiebenden Schichten. Bachelor's Thesis, University of Mainz, Mainz, Germany, 2018. Available online: https://butler.physik.uni-mainz.de/icecube/thesis/bachelor_Lucas_Binn.pdf (accessed on 26 January 2022).
33. Norland. NOA 148H. 2021. Available online: https://www.norlandprod.com/adhesives/NOA148.html (accessed on 26 January 2022).
34. Falke, P. Entwicklung Eines Lichtkonzentrators Basierend Auf Einer Hohlzylinder Geometrie. Bachelor's Thesis, Universität Bonn, Bonn, Germany, 2014.
35. Schnur, R. Optimierung des Adiabatischen Lichtleiters für das Wavelength-Shifting Optical Module. Bachelor's Thesis, Johannes Gutenberg-Universität Mainz, Mainz, Germany, 2020. Available online: https://butler.physik.uni-mainz.de/icecube/thesis/bachelor_Ronja_Schnur.pdf (accessed on 26 January 2022).
36. Hebecker, D. Development of a Single Photon Detector Using Wavelength-Shifting and Light-Guiding Technology. Ph.D. Thesis, Humbold-Universität Berlin, Berlin, Germany, 2021. Available online: https://edoc.hu-berlin.de/handle/18452/23885?locale-attribute=de (accessed on 26 January 2022).
37. Schlickmann, L. Zeitantwort des Wellenlängenschiebenden Optischen Moduls (WOM). Master's Thesis, Johannes Gutenberg University Mainz, Mainz, Germany, 2021. Available online: https://butler.physik.uni-mainz.de/icecube/thesis/bachelor_SchlickmannLea.pdf (accessed on 26 January 2022). (In German)
38. Bubeck, M. Developement of a Wavelength-Shifting Optical Module. Master's Thesis, Johannes Gutenberg University Mainz, Mainz, Germany, 2020; p. 19. Available online: https://butler.physik.uni-mainz.de/icecube/thesis/master_Maximilian_Bubeck.pdf (accessed on 26 January 2022).
39. Rea, I.C.; Holzapfel, K.; Baron, A.; Bailly, N.; Bedard, J.; Bohmer, M.; Bosma, J.; Brussow, D.; Cheng, J.; Clark, K.; et al. P-ONE second pathfinder mission: STRAW-b. *PoS* **2021**, *ICRC2021*, 1092. [CrossRef]
40. Ehlert, M.; Hollnagel, A.; Korol, I.; Korzenev, A.; Lacker, H.; Mermod, P.; Schliwinski, J.; Shihora, L.; Venkova, P.; Wurm, M. Proof-of-principle measurements with a liquid-scintillator detector using wavelength-shifting optical modules. *JINST* **2019**, *14*, P03021. [CrossRef]
41. SHiP Collaboration. The SHiP experiment at the proposed CERN SPS Beam Dump Facility. *arXiv* **2021**, arXiv:2112.01487.
42. Rack-Helleis, J.; Pollmann, A.; Rongen, M. The Wavelength-shifting Optical Module (WOM) for the IceCube Upgrade. *PoS* **2021**, *ICRC2021*, 1038.